AIAA Journal
Vol. , No. ,

Aerodynamic and Aeroacoustic Optimization of Leading-Edge Undulation of a NACA 65(12)-10 Airfoil

Jung-Hoon Kim* and Kwing-So Choi†
University of Nottingham, Nottingham, England NG7 2RG, United Kingdom
Giovanni Lacagnina,‡ Chaitanya Paruchuri,§ and Phillip Joseph¶
University of Southampton, Southampton, England SO17 1BJ, United Kingdom
S. M. Hasheminejad**
Iran University of Science and Technology, 13114-16846 Tehran, Iran
Tze Pei Chong††
Brunel University London, Uxbridge, England UB8 3PH, United Kingdom
M. F. Shahab‡‡
DHA Suffa University, Karachi 75500, Pakistan
and
Mohammad Omidyeganeh§§ and Alfredo Pinelli¶¶
City University of London, London, England EC1 V 0HB, United Kingdom

https://doi.org/10.2514/1.J060716

1 **Experimental studies of a NACA 65(12)-10 airfoil with a sinusoidal leading-edge undulation (LEU) were carried out to simultaneously optimize its aerodynamic and aeroacoustic performances by considering the attached as well as the separated flow at the effective Reynolds number of 10^6, where the maximum lift was increased without sacrificing drag or overall noise near- and poststall angles. Further aerodynamic and aeroacoustic tests indicated that a combination of LEU wavelength $\lambda/c = 30\%$ and amplitude $h/c = 6\%$ gave an optimum LEU by considering the aerodynamic performance as well as the noise reduction. Particle image velocimetry measurements of the flow over the optimized airfoil showed biperiodic velocity fluctuations downstream of the LEU peaks that were associated with unsteady stall cell structure near the trailing edge.**

Nomenclature

A	=	planform area
C_D	=	drag coefficient, $2D/\rho U_\infty^2 A$
C_L	=	lift coefficient, $2L/\rho U_\infty^2 A$
$C_{L,\max}$	=	maximum lift coefficient
c	=	chord length, mm
c_m	=	mean chord length, mm
D	=	drag force, mm
f	=	frequency, Hz
h	=	peak-to-peak amplitude of leading-edge undulation, mm
L	=	lift force, N
OAPWL	=	overall sound power level, dB
PWL	=	sound power level, dB
Re_c	=	Reynolds number based on the chord length, $U_\infty c/\nu$
St	=	Strouhal number, fc/U_∞
s	=	span, mm
U_∞	=	freestream velocity, m s^{-1}
u'	=	root mean square of streamwise velocity fluctuations, m s^{-1}
x	=	chordwise coordinate of the baseline airfoil, mm
α	=	angle of attack
α_{eff}	=	effective angle of attack
λ	=	wavelength of the leading-edge undulation, mm
ν	=	kinematic viscosity, m^2 s^{-1}
ξ	=	chordwise coordinate of the leading-edge undulation, mm
ρ	=	density, kg m^{-3}

I. Introduction

FLOW control methods have often been inspired by nature [1,2]. Among those, flippers of humpback whales have drawn much attention of researchers recently due to their outstanding hydrodynamic performance [3], where it was mentioned in [3] that the leading-edge undulation (LEU) of flippers helps them bank and turn sharply to catch their prey. During the wind tunnel experiments of flipper models, increased $C_{L,\max}$ with a delayed stall was observed [4]. Since then, various geometric parameters of the LEU affecting 2
the airfoil performance were investigated. Johari et al. [5] studied the aerodynamic effect of the LEU wavelength and amplitude of NACA 63_4-021 airfoils with an aspect ratio of 2 and the chord Reynolds number $Re_c = 1.8\times10^5$. Their results were compared to the airfoil with a straight leading edge (SLE) to show that C_L increase was obtained only in poststall angles. Further investigations were made in [6] with various planforms of NACA 63_4-021 at a wide range of Re_c, showing that there is a certain combination of the LEU wavelength and amplitude to give an increase in C_L. However, no comparison of C_L was presented for full span models with these LEU parameters. In [7], aerodynamic characteristics of the LEU on NACA 63_4-021 airfoils of an aspect ratio of 4 were examined at $Re_c = 1.8\times10^5$, where an airfoil with a sinusoidal LEU showed higher maximum lift at smaller stall angle than the airfoil with SLE.

Presented as Paper 2021-1293 at the AIAA SciTech 2021 Forum, Virtual Event, January 11–21, 2021; received 17 March 2021; revision received 5 October 2021; accepted for publication 12 October 2021; published online Open Access XX epubMonth XXXX.

*Research Fellow, Faculty of Engineering.
†Professor, Faculty of Engineering. Associate Fellow AIAA.
‡Research Fellow, Institute of Sound and Vibration Research.
§Lecturer, Institute of Sound and Vibration Research.
¶Professor, Institute of Sound and Vibration Research.
**Research Fellow.
††Reader, Department of Mechanical and Aerospace Engineering. Member AIAA.
‡‡Assistant Professor, Department of Mechanical Engineering.
§§Lecturer, School of Mathematics, Computer Science and Engineering.
¶¶Professor, School of Mathematics, Computer Science and Engineering.

Hansen et al. [8] tested different symmetric airfoils (NACA 0012 and NACA 65-021) with LEUs at $Re_c = 1.2 \times 10^5$. They showed that $C_{L,\max}$ was more sensitive to the amplitude than the wavelength of LEU, although no increase in lift was observed. Rostamzadeh et al. [9] investigated NACA 0021 airfoils with a wavy leading edge whose geometric angle of attack changed sinusoidally in the spanwise direction. These wavy airfoils outperformed the airfoil with an SLE in poststall angles but $C_{L,\max}$ was never increased.

Cambered airfoils with LEUs have also been examined for engineering applications. For a micro-air vehicle application, effects of amplitude and wavelength of sinusoidal LEUs on a NASA LS(1)-0417 airfoil with a low aspect ratio were studied in [10]. Two-dimensional, infinite-span cascades of NACA 4415 and NACA 0015 profiles with LEUs were numerically investigated, where it was shown that the airfoil camber has a strong influence on the aerodynamic performance [11]. This work was extended to a ventilation fan with ARA-D airfoils in [12], where the wavelength and the amplitude were redesigned to improve the poststall characteristic. A single swept-back SD7032 airfoil with an LEU was examined at $Re_c = 5.5 \times 10^4$ in [13], where a C_L increase over an entire angle of attack tested was reported. A summary of recent research on cambered NACA airfoils with LEUs is given in [14]. A NACA 65(12)-10 airfoil with different LEUs was investigated recently [15] with a view to develop a new scaling law of lift coefficient to explain the reduction in the lift slope.

The aeroacoustic effects of LEUs are also reported in a number of papers. Turbulence–airfoil interaction noise was reduced by 3–4 dB using an LEU [16], whereas studies of a flat plate LEU in [17] showed that the optimum wavelength should have approximately four times the transverse integral-length scale of the freestream turbulence. It also showed that LEUs were effective in reducing the airfoil self-noise. Hansen et al. [18] reported that the tonal noise and broadband noise from a NACA 0021 airfoil with $Re_c = 120{,}000$ were significantly reduced at the angle of attack of between 5 and 8°. Similar results are reported in [19] where the tonal noise due to laminar flow instability from a NACA 65(12)-10 airfoil was suppressed by LEU.

In many studies (e.g., [8,20–23]), counter-rotating streamwise vortices have been observed downstream of the LEU, which are considered to be related to the C_L increase in poststall angles. Their downstream developments are summarized in [20,24–26]. For symmetric airfoils, the design of LEU is rather simple since its leading edge always stays on the chord line, which coincides with the mean camber line. For cambered airfoils, however, there are a number of possibilities in designing the LEU, but only few studies have looked at the effect of LEU shape and location, which is the main objective of this paper. Here, LEUs were made by cutting into the airfoil so that an extrapolation of the camber line is unnecessary [19]. Aerodynamic optimization and aeroacoustic optimization of LEU were then carried out to obtain the best performing leading-edge profile. Measurements of the flow around an airfoil were also made using particle image velocimetry (PIV) to understand the mechanism behind the performance improvement with an optimized LEU.

II. Experimental Setup

A. Aerodynamic Measurements

Aerodynamic measurements were carried out in an open-return wind tunnel at the University of Nottingham, whose test section measured 0.91 m wide ×0.75 m high ×1.5 m long. NACA 65(12)-10 airfoils with and without sinusoidal LEU were manufactured by a 3D printer, Zortrax M300 using Z HIPS (high-impact polystyrene) and polished with P120 and P600 sandpapers. Therefore, the surface finish of the airfoil models is estimated to be $Ra = 0.23$ μm. They were vertically positioned between two endplates at the center of the wind-tunnel test section, 0.1 m above the tunnel floor and 0.7 m downstream from the inlet. The bottom endplate consisted of a 150-mm-diam circular plate that was rotated with an airfoil model around a 360 mm × 260 mm stationary rectangular plate, which was attached to the tunnel floor (see Fig. 1). The identically shaped upper endplate was attached to the wind tunnel ceiling with a 2 mm gap from the tip of the airfoil model. The leading and trailing edges of both endplates had a super-elliptic shape to avoid local flow separation.

To increase the effective Reynolds number to 10^6 [27] during the aerodynamic measurements, a 20 mm × 20 mm square-hole perforated plate (the grid) with a 25 mm pitch (64% porosity) was installed 0.56 m (22 grid pitches) upstream of the airfoil model, with which the turbulence intensity and the turbulence integral scale in the freestream were increased to 4.3% and 13 mm, respectively. Here, the turbulence integral scale was obtained using the method described in [28]. The ratio of turbulence length scale to the airfoil thickness was of the order of 1, which was found effective in reducing the size of laminar separation bubble over an airfoil [29]. Without the grid, the turbulence intensity in the freestream was 0.3%, where the chord Reynolds number was $Re_c = 10^5$.

The use of turbulence-generating grid was aimed at removing the ambiguity in aerodynamic measurements at low to medium Reynolds numbers, where the aerodynamic forces on airfoils are strongly influenced by the boundary-layer transition [30]. Indeed, much of the confusion in the past studies is a result of this, because the LEU undulation often triggers boundary-layer transition, resulting in a flow separation delay accompanied by an increase in the lift coefficient and/or the maximum lift angle. This was often confused with an improvement in aerodynamics performance by the introduction of LE undulation. The increased freestream turbulence by grid will increase the effective Reynolds number by promoting transition to turbulence closer to the leading edge of the airfoil. Here, the effective Reynolds number is the equivalent Reynolds number in the airfoil aerodynamic tests when the freestream turbulence level is nearly zero [27]. The use of turbulence-generating grid is similar to but more effective than the trip devices in promoting the boundary-layer transition.

A three-component force transducer (Kyowa, LSM-B-SA1, rated capacity 10 N) was used to measure the drag and lift forces of airfoil models. The force balance was mounted on a turntable that was connected through a 2∶1 gear to a stepping motor to reduce the minimum angle of rotation to 0.45 deg. The data from the force

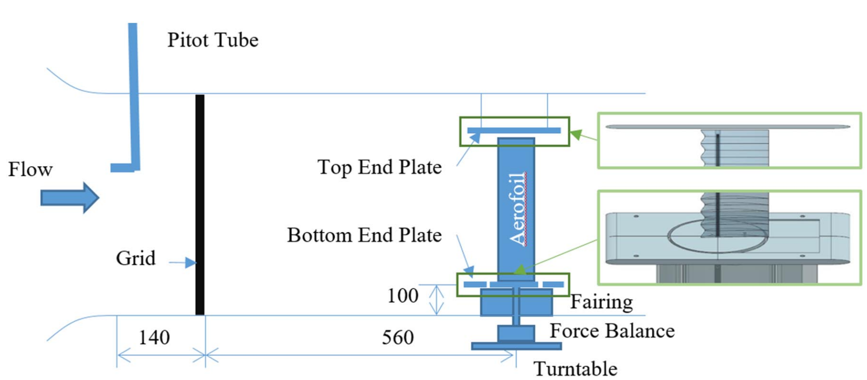

Fig. 1 Experimental aerodynamic measurement setup (not to scale). Units are in mm.

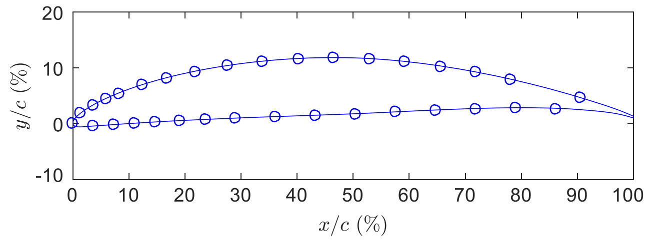

Fig. 2 Positions of the pressure taps on the airfoil model.

balance were acquired with a 16-bit analog-to-digital (A/D) converter (IOtech ADC488/8SA) for 30 s at the sampling frequency of 500 Hz.

For surface pressure measurements, an airfoil model with a 150 mm chord length and a 500 mm span was designed and 3D printed, including 19 and 15 pressure taps of 0.8 mm in diameter along the centerline over the upper (suction) and the lower (pressure) surfaces, respectively (see Fig. 2). Unfortunately, one of the pressure taps was blocked during printing, so that the surface pressure measurement between $x/c = 80$ and 90% could not be made. We used National Instruments (NI) LabVIEW software for pressure measurements, controlling a pressure scanner (Scanivalve MPS4264, full scale range ±995.4 Pa) incorporating 24-bit A/D converters. The data were acquired at 800 Hz for 1 minute, which were then transferred to a PC through an Ethernet cable.

The PIV system consisted of a Litron LDY302-PIV Nd:YLF laser with 15 mJ per pulse, two high-speed cameras (Phantom v12.1) with Sigma 105-mm-focal-length lenses, an NI 80N77 Timer Box, and a dedicated PC. Di-ethyl-hexyl-sebacat (DEHS) seeding particles of nominally 1 μm diameter were introduced upstream of the wind tunnel contraction section using a TSI 9307-6 seeding generator via a seeding rake. A laser sheet horizontally illuminated the airfoil section near the midspan. The field of view of two cameras set side by side was 172 mm × 55 mm, which captured the entire flowfield around the airfoil. The twin-cavity laser was operated for 2.5 s to obtain image pairs at a repetition rate of 1600 Hz with a 40 μs time delay between two consecutive pulses. The particle images were used to produce velocity vectors by an adaptive PIV algorithm using Dynamic Studio v 4.15 software, where the window shift, subpixel interpolation, and window deformation were also carried out. Here, the size of the interrogation area was automatically adapted between 32 and 64 pixels horizontally and 16 and 32 pixels vertically to make sure that the desired number of particles per interrogation area remained around 10. The overlap ratio varied between 50 and 75%.

Uncertainties in the measured freestream velocity, aerodynamics
3 forces, and airfoil alignment are ±0.5% FS, ±0.3% FS, and ±0.3°, respectively, giving maximum experimental errors in the lift and drag coefficients of 2.5 and 13.2%, respectively [31]. The accuracy of the pressure scanner is ±0.15% FS so that the maximum experimental error in the pressure coefficient is estimated to be 2%. The error in PIV measurements is estimated using the equation $\sigma_{\Delta x} = kd_\tau$ [32], where $\sigma_{\Delta x}$ and d_τ are the standard deviation of subpixel displacement and image diameter in pixel, respectively. Also, $k = \eta D_I/(2\gamma N_I^{0.5})$, where η, D_I, γ, and N_I are the standard deviation of noise in grayscale value, geometric mean of interrogation area in pixel, averaged exposure of a single particle in grayscale value, and image density, respectively, of the particle images. For the present study, the averaged image diameter was $d_\tau = 1.28$ pixels, which is close to the optimum particle diameter of 2 pixels in [32]. Considering the minimum interrogation window size of 32 × 16 pixels, η, D_I, γ, and N_I are estimated to be 1.4, 22.6, 51, and 6.4, respectively. Therefore, $k = 0.13$, so that $\sigma_{\Delta x} = kd_\tau = 0.16$ pixel. Total uncertainty in mean and root mean square velocity can be given by $\varepsilon_{t,\overline{U}} = u'/\sqrt{N}$ and $\varepsilon_{t,u'} = \sqrt{\sigma_{\Delta x}^2 + (u'/\sqrt{2N})^2}$, respectively, where N is a number of samples averaged [33]. Therefore, experimental uncertainties in $\overline{U}/U_\infty$ and u'/U_∞ are 1 and 6.6%, respectively, with a 95% confidence.

B. Aeroacoustic Measurements

Acoustic measurements of airfoils were carried out in an open-jet wind tunnel facility at the Institute of Sound and Vibration Research (ISVR) of the University of Southampton (see Fig. 3). The wind tunnel was housed in an anechoic chamber measuring 8 m × 8 m × 8 m, whose walls were acoustically treated with glass-wool wedges to reach the lowest cutoff frequency of 80 Hz. A large nozzle, 500 mm high and 350 mm wide, was used to minimize the incident flow deflection by the airfoil, where two side plates were attached to maintain the two-dimensionality of the flow. The angle of attack was corrected according to the formula in [34] to give an effective angle of attack, α_{eff}, which was approximately 35% less than the geometric angle of attack. A biplanar rectangular grid located 75 cm upstream of the nozzle exit was used to generate freestream turbulence, whose intensity and the integral length scale were 2.5% and 7.5 mm, respectively, in the measurement section.

An array of 10 half-inch condenser microphones (B&K type 4189), located 1.2 m from the midspan of the airfoil, was used to take free-field noise measurements. The emission angles of microphones relative to the downstream direction of the jet axis were in the range of 40–130 deg. Each noise measurement lasted for 20 s at a sampling frequency of 40 kHz. The uncertainty in the noise measurement using these microphones was ±0.2 dB. A further detail of this facility and the test equipment used can be found in [35,36].

III. Results

A. Characteristics of the Baseline Model

Figure 4 shows the lift coefficient C_L and the drag coefficient C_D of the baseline model against the angle of attack α, where error bars are shown to indicate the maximum experimental errors. At the chord Reynolds number of $Re_c = 10^5$ without grid, the C_L curve shows a nonlinear behavior that is typical of low-Reynolds-number flows [37–40], where the lift slope is initially low ($0 < \alpha < 4°$) and then increased until $\alpha = 10°$. The C_L will then drop sharply after the

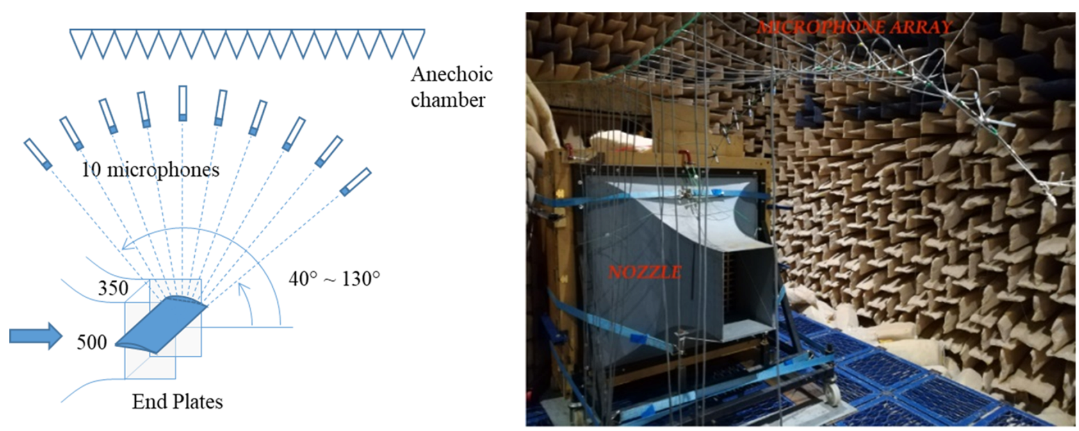

Fig. 3 Open-jet wind tunnel and the acoustic setup inside the ISVR's anechoic chamber.

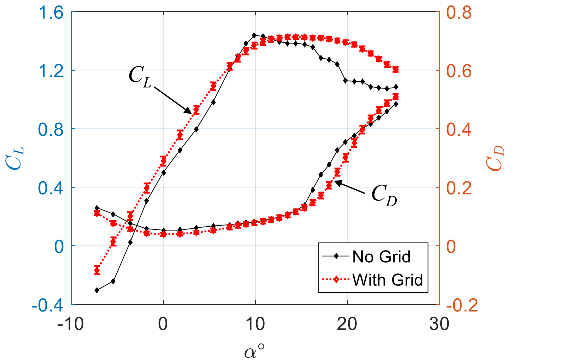

Fig. 4 Lift and drag coefficients of the baseline model with and without grid.

maximum lift angle. This behavior is believed to be due to separation bubbles formed over both sides of the airfoil [41–43], which will be discussed later. When we test the airfoil at the effective Reynolds number of 10^6 with grid, on the other hand, the C_L increased linearly with α up to 5° ($C_L = 1.1$) to reach the maximum lift coefficient $C_{L,\max}$ at around $\alpha = 14.5°$.

The behavior of the pressure coefficient C_p over the same airfoil without grid, as shown in Fig. 5a, suggests that a large separation bubble was formed near the leading edge over the lower surface (LS), creating a negative pressure region between $x/c = 3\%$ and 30% at $\alpha = -1.8°$. The lower surface of NACA 65(12)-10 airfoil is nearly flat; therefore it is susceptible to flow separation at negative angles of attack at low Reynolds number. At the effective Reynolds number of 10^6 with grid, the negative pressure region seems to be eliminated. The C_p distribution without grid, shown in Fig. 5b, suggests an early flow separation over the upper surface at $\alpha = 5.4°$, leading to a low C_L value (see Fig. 4). With grid, the static pressure over the upper surface remains low up to the 80% chord, increasing the C_L. A kink in the Cp distribution without grid as shown in Fig. 5c suggests a laminar separation bubble [44,45] over the upper surface of the airfoil between $x/c = 60$ and 80% at $\alpha = 9.9°$, which helps increase the C_L until it finally bursts at around $\alpha = 16°$ (see Fig. 4). Again, the stall angle is delayed with grid beyond the angle of attack of $\alpha = 20°$, which is accompanied by an increase in C_L by more than 20%. A nearly flat C_p distribution over the upper surface of the airfoil without grid at $\alpha = 19.8°$ (see Fig. 5d) suggests that a global flow separation is taking place, whereas the leading-edge flow separation seems to be delayed with grid.

B. Optimization of Leading-Edge Profile

1. Cross-Sectional Profiles of Leading-Edge Undulation

Optimization of the leading-edge profile was carried out for a NACA 65(12)-10 airfoil with a 100 mm chord length and a 500 mm span, where the LEU amplitude and wavelength were 6 and 20% of the chord length, respectively (see Fig. 6a). Due to manufacturing constraints, the trailing edge of the airfoil was rounded with a radius equivalent to 0.5% of the chord length. Therefore, the trailing edge did not extend to the "true" chord line of this airfoil. LEUs were cut into the baseline profile rather than added to it.

We considered three types of leading-edge profiles: Und1, UAC, and UMC, indicating undulation 1, undulation along the camber, and undulation with a modified camber, respectively. Figure 6b shows the Und1 profile, where the cross-sectional profile of the LEU is similar to that of the base line profile, whose leading edge always stays along the chord line within the LEU. On the other hand, the UAC profile, as shown in Fig. 6c, is obtained by modifying only the 24% of the original leading-edge section by maintaining a similar shape. To be aerodynamically efficient, the LEU must be positioned upstream of the maximum camber for cambered airfoils [12] or the maximum thickness for symmetric airfoils [5]. If it is too upstream, however, the curvature of modified leading-edge profile becomes too large, leading to local flow separation. The location of LE undulation ($x/c = 24\%$) in this study was chosen by considering that the maximum camber and the maximum thickness of the NACA 65(12)-10 airfoil are 51 and 42%, respectively. Here, the mean

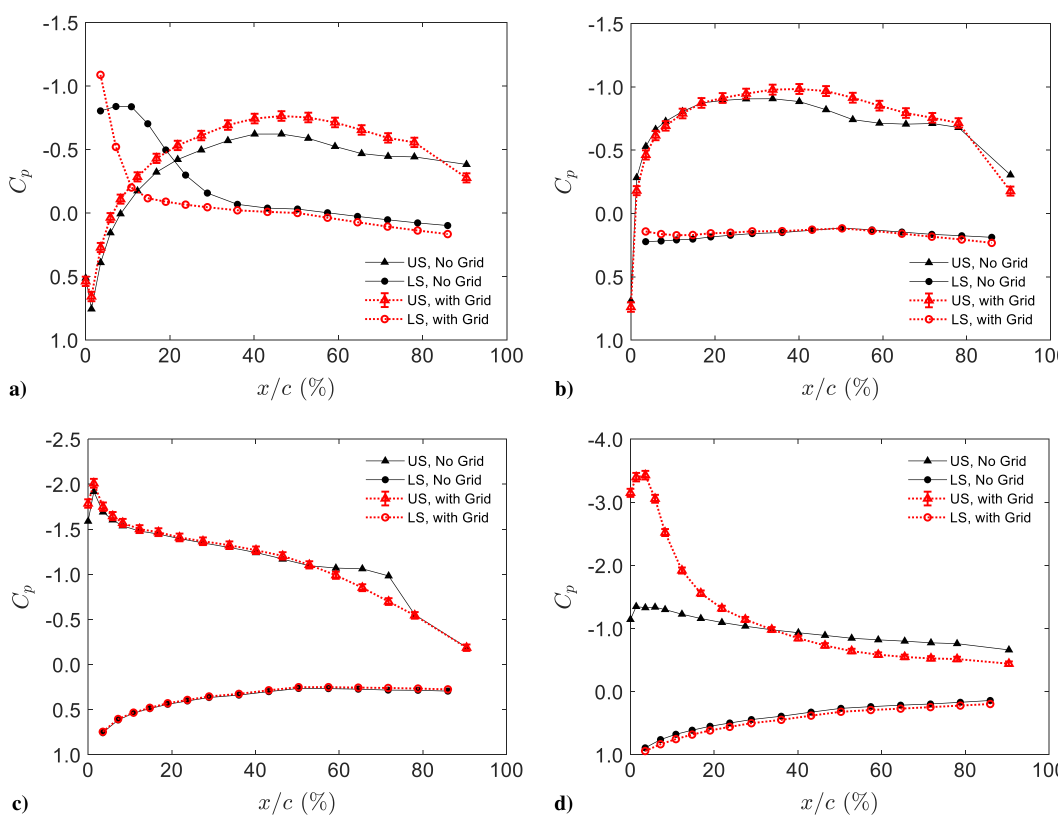

Fig. 5 C_p distributions on the upper surface (US) and the lower surface (LS) at α equal to a) −1.8°, b) 5.4°, c) 9.9°, and d) 19.8°. Error bars to indicate experimental uncertainties are shown in (a).

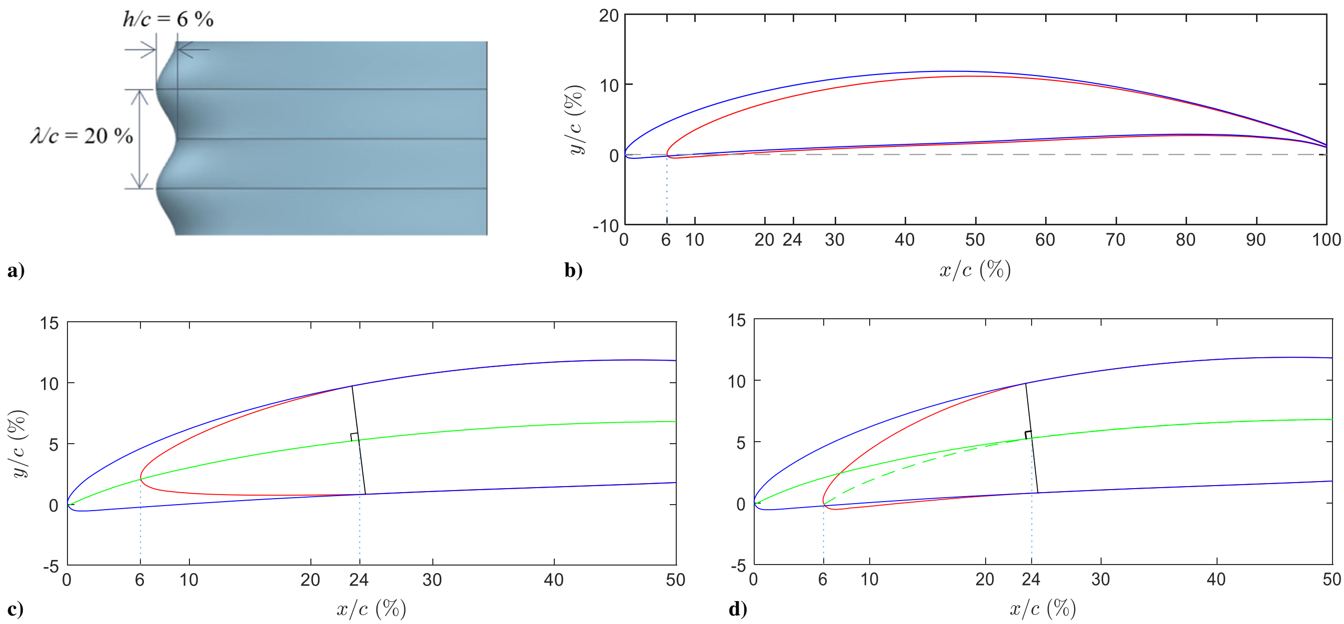

Fig. 6 Definition of the amplitude and wavelength of the leading-edge undulation (a), and the profiles of Und1 (b), UAC (c), and UMC (d) showing camber lines at the peak (blue) and trough (red) sections.

camber line of the UAC profile always stays on the original mean camber line within the LEU. The mean chord position ξ of the UAC profile measured from its local leading edge can be expressed by the original chord position x in a simple linear relationship, given by Eq. (1).

$$\left(\frac{\xi}{c}\right) = \frac{3}{4}\left(\frac{x}{c}\right) + 6 \tag{1}$$

Similar to the UAC profile, the leading-edge shape of the UMC profile changes only the front 24% of the original airfoil section (see Fig. 6d). However, the leading edge of the UMC profile stays along the chord line within the LEU. In this case, the $x-\xi$ transformation of the mean camber line can be given by a third-order polynomial given by Eq. (2).

$$\left(\frac{\xi}{c}\right) = a_0\left(\frac{x}{c}\right)^3 + \left(\frac{1}{96} - 48a_0\right)\left(\frac{x}{c}\right)^2 + \left(576a_0 + \frac{1}{2}\right)\left(\frac{x}{c}\right) + 6 \tag{2}$$

Here, the polynomial constants were determined by imposing conditions that the slope of the mean camber line is 6° at the modified leading edge and that $d\xi/dx = 1$ at $x/c = 24\%$ to avoid a discontinuity in the slope of the mean camber line. We also required that $\xi/c = 6\%$ at $x/c = 0$ and $\xi/c = 24\%$ at $x/c = 24\%$. We then found that the numerical constant in Eq. (2) is given by $a_0 = 5.2 \times 10^{-4}$. It should be noted that the UAC and UMC thickness associated with the $x-\xi$ transformation in Eqs. (1) and (2) should be measured normal to the mean camber line, not normal to the chord line.

2. *Lift and Drag Coefficients*

C_L and C_D of airfoils with the leading-edge profile Und1, UAC, and UMC are now presented along with those of the baseline (BL) in Fig. 7a. Here, the lift and drag coefficients are defined based on the actual planform area of the modified airfoil with LE undulation. It shows that the UMC profile outperforms the UAC and Und1 profiles in the C_L enhancement in both pre- and poststall conditions. Additionally, the enhancement in C_L by the UMC profile is accompanied by a reduction in C_D. This superior aerodynamic performance of UMC profile can be observed either with grid (see Fig. 7a) or without grid (see Fig. 7b), which can be explained as follows.

The leading edge of the UMC profile stays along the chord line within the LEU (see Fig. 6d), so that the local angle of attack of the LEU is always less than that of the baseline profile. As a result, the suction peak near the leading edge of the airfoil would be reduced by this LEU, which helps increase C_L by delaying flow separation. The Und1 profile also increases C_L, but the increment is limited only to poststall angles. Although similar to the UMC profile in design, the leading edge of the UAC profile is located along the mean camber line within the LEU; therefore the local angle of attack is always greater than that of UMC.

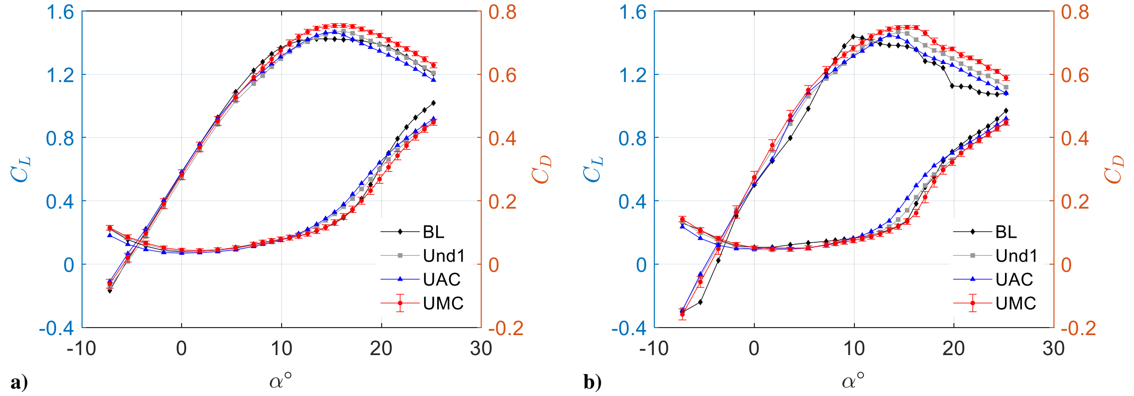

Fig. 7 Comparisons of C_L and C_D between different LEU shapes a) with grid and b) without grid.

Figure 7 also demonstrates that the UMC profile increases the $C_{L,\max}$ more than that of the baseline with a similar level of C_D. Such an aerodynamic performance improvement was never seen by any LEUs before [6,8,23]. Previous reports showing an increase in $C_{L,\max}$ with LEUs were either by an airfoil with a small aspect ratio [6] or by a tapered airfoil [4], both of which have strong flow three-dimensionality over the airfoil. Also, a 10% increase in $C_{L,\max}$ with an LEU on NACA $63_4 - 021$ airfoil reported in [7] was achieved with an expense of 50% increase in C_D.

3. Sound Power Level and Spectra

Figure 8 shows overall sound-power level (*OAPWL*) variations with the effective angle of attack α_{eff} for the baseline (BL) and an airfoil with three different LEUs (Und1, UAC, and UMC) in a freestream of 20 m/s, corresponding to the chord Reynolds number of $Re_c = 1.3 \times 10^5$ without grid. Here,

$$\text{OAPWL} = 10\log_{10} \int_{f_1}^{f_2} 10^{\frac{\text{PWL}(f)}{10}} \, \mathrm{d}f \tag{3}$$

where $\text{PWL}(f)$ is the sound power level that is calculated by integrating the sound pressure power spectral densities measured at every 10° between 40 and 130° of the polar angles in Fig. 3. These data were obtained by integrating the noise spectra between 40 and 2000 Hz, covering both the separation noise and the stall noise [36]. For the case of with grid, it is clear that the noise in the entire frequency range considered is reduced from the baseline (BL) level by employing LEUs. In particular, noise reductions by LEUs are enlarged further in the effective angle of attack α_{eff} ranging between 12 and 18° where the lifts of the airfoils reach nearly maximum (see Fig. 7a). For "no grid" cases, however, noise is increased by LEUs except for $\alpha_{\text{eff}} < \sim 5°$, where the laminar boundary-layer instability (Tollmien–Schlichting waves) noise is amplified by the separation bubble [46]. Here, the boundary-layer instability noise is identified as a hump in the Strouhal number St between 1 and 10 in the spectrum for $\alpha_{\text{eff}} = 3.7°$ in Fig. 9. A wide and low hump is also seen in the spectrum for $\alpha_{\text{eff}} = 3.7°$ with grid (see Fig. 9). The boundary-layer instability noise is thought to become weaker with grid because the separation bubble would be much smaller or eliminated, as implicated by the C_p distribution in Fig. 5b for x/c between 60 and 90%. Figure 9 also shows that at α_{eff} near stall ($\alpha_{\text{eff}} = 14.8°$), the amplitude near $St = 1$ increases and the hump is reduced or stops increasing with or without grid. Past the stall ($\alpha_{\text{eff}} = 22.3°$), the power spectral amplitude of St less than around 0.5 is only seen to increase.

To see the effect of LEUs on different frequency components, power spectra of airfoils with LEUs subtracted from the baseline data are presented in Fig. 10 at different α_{eff}. It is clear from Fig. 10a that all LEUs at low α_{eff} reduced the laminar boundary-layer instability noise for St between 1 and 10 for "no grid" case. However, in the low

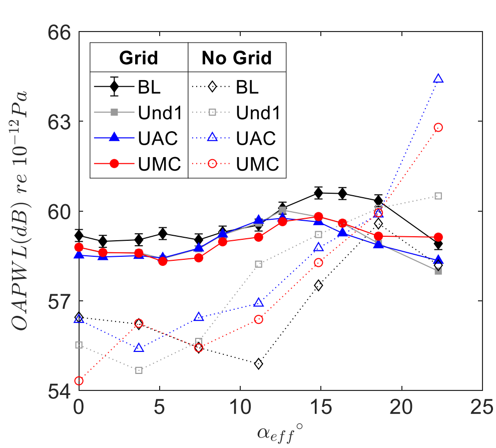

Fig. 8 Overall-sound-power-level variations with the attack angle of the airfoils. The amplitude and the wavelength of the LE undulation are 6 mm ($h/c = 6\%$) and 20 mm ($\lambda/c = 20\%$), respectively.

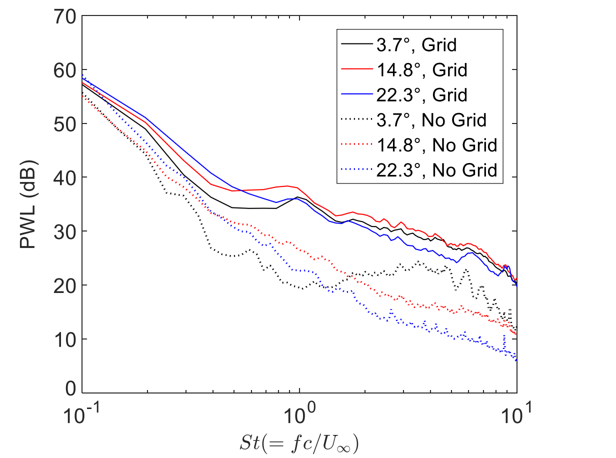

Fig. 9 Sound power spectra for the baseline airfoil at three representative angles of attack with and without the grid.

St range between 0.2 (40 Hz) and 1 (200 Hz), where large portions of acoustic energy were contained, the noise was increased by LEUs and these increases are greatest with the UMC profile followed by UAC and Und1. With grid, there was as much noise increase in the lower range of St, whereas there were small decreases in higher St range. Near stall, Fig. 10b demonstrates that the noise reduction effects by LEUs with grid are seen in the entire frequencies except for near $St = 1$. In Fig. 10c, it is seen that the noise in lower St range increased greatly for "no grid" case due to stall at this angle of attack of $\alpha_{\text{eff}} = 22.3°$.

C. Optimization of Amplitude and Wavelength

Aerodynamic performance and aeroacoustic performance of NACA 65(12)-10 airfoils with Und1, UAC, and UMC leading-edge profiles were presented in the previous section, where the UMC profile demonstrated the highest C_L with the lowest C_D near and poststall angles. All LEUs tested reduced the laminar boundary-layer instability noise at low effective angle of attack α_{eff} in a low-turbulence freestream (i.e., with "no grid"). They also reduced the overall sound power level near the stall angle in a high turbulence freestream with grid. Using this best performing UMC profile we have carried out a further optimization of LEUs to find the best combination of LEU amplitude h and wavelength λ using a 3×3 test matrix in h (3, 6, and 12% chord) and λ (10, 20, and 30% chord).

1. Maximum Lift Enhancement

C_L and C_D of the UMC profile in a 3×3 test matrix are presented in Fig. 11. Here, each LEU configuration is named by the percentage value of wavelength and amplitude in chord length, e.g., $\lambda 10h3$ indicates an LEU with 10% λ/c and 3% h/c. Figures 11a–11c clearly show that C_L and C_D with grid depended strongly on a combination of the LEU wavelength and amplitude. For a low LEU wavelength ($\lambda/c = 10\%$), C_L is reduced with an increase in the LEU amplitude from $h/c = 3$ to 12%, as seen in Fig. 11a. Compared to the baseline, C_L is greater with the LEU of a small amplitude $h/c = 3\%$, but only at near-stall angles. C_D is decreased by the LEU with all amplitudes tested. With a medium LEU wavelength ($\lambda/c = 20\%$) the maximum lift coefficient $C_{L,\max}$ is increased by all LEUs, as shown in Fig. 11b. For a large LEU wavelength ($\lambda/c = 30\%$), as shown in Fig. 11c, C_L at near and poststall angles is increased with an increase in the LEU amplitude, which is offset by an increase in C_D, however. For example, a 13% increase in C_L by the LEU with $h/c = 12\%$ is achieved by $\lambda 30h12$ with an expense of a 24% increase in C_D (see Fig. 11c). Similar observations are made with "no grid" cases in Figs. 11d–11f, where not smooth C_L and C_D curves as compared to those "with grid" are due to laminar separation bubbles (see discussions in Sec. III.A).

Figures 12a and 12b are contour maps to show the percentage increase in $C_{L,\max}$ of the UMC profile against the baseline with and

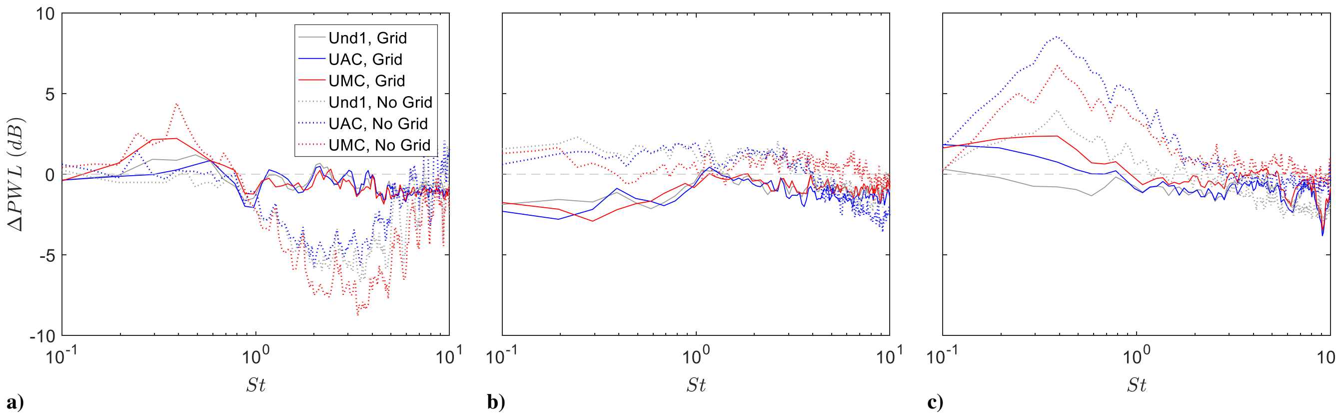

Fig. 10 Sound power spectra of the airfoils with the LEU subtracted from those of the baseline at $\alpha_{\mathrm{eff}} = 3.7°$ (a), 14.8° (b), and 22.3° (c).

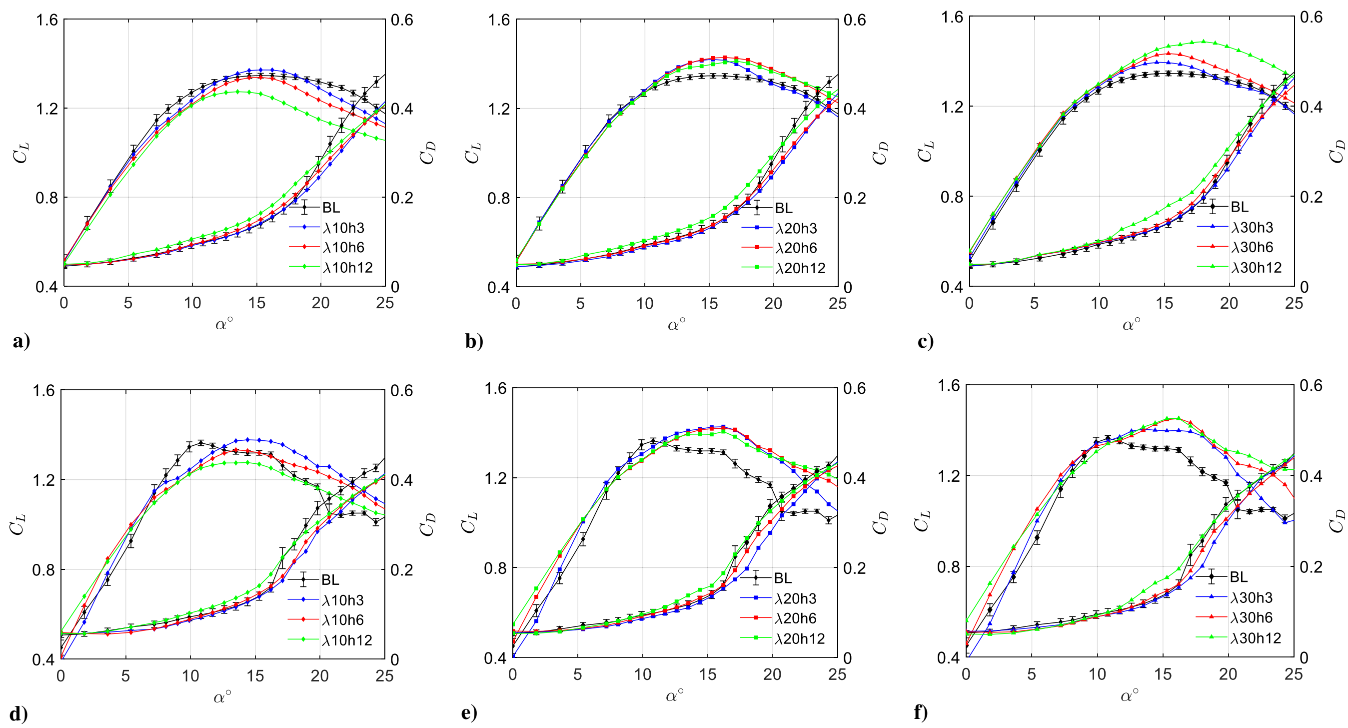

Fig. 11 C_L and C_D of UMC leading-edge profile with various h and λ against α: a–c) with grid; d–f) without grid. The baseline data are also shown for comparison. The legends in the figure represent the percentage value of each parameter; e.g., λ10h3 indicates an LEU with 10% λ/c and 3% h/c.

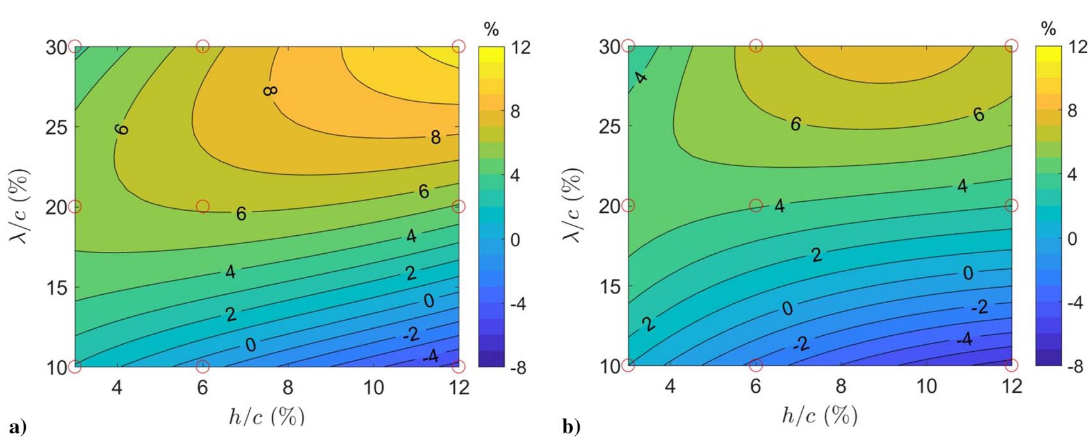

Fig. 12 Contour maps to show the percentage increase in $C_{L,\max}$ of the UMC profile based on a 3 × 3 test matrix of h and λ: a) with grid; b) without grid.

without grid, respectively, which were obtained from a 3 × 3 test matrix of different LEU amplitudes ($h/c = 3$–12%) and wavelengths ($\lambda/c = 10$–30%). The contour maps were obtained by interpolating 9 $C_{L,\max}$ values (shown by red circles) from Fig. 11. In both figures the local maximum of $C_{L,\max}$ can be found in the top-right-hand corner of the contour map, suggesting that the optimum LEU for $C_{L,\max}$ should have greater wavelength and amplitude with or without grid.

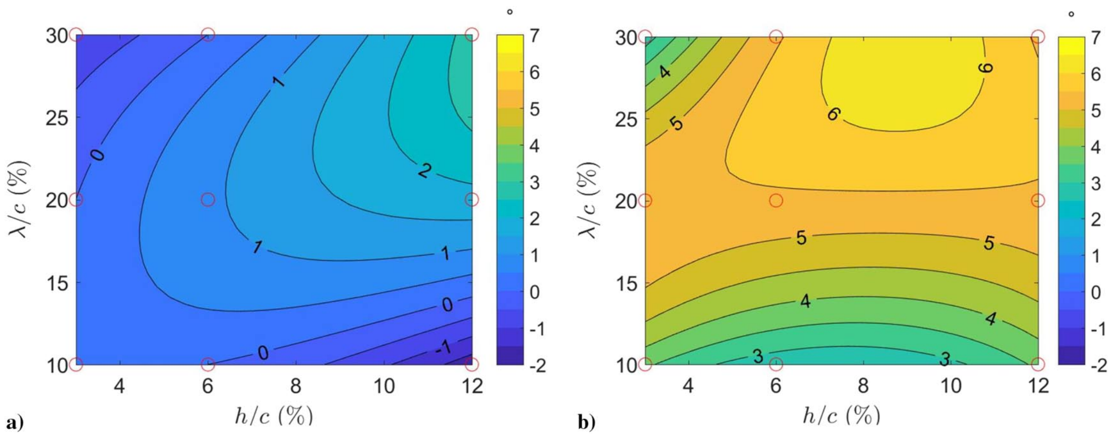

Fig. 13 Contours to show the percentage increase in the maximum lift angle of the UMC profile based on a 3 × 3 test matrix of h and λ: a) with grid; b) without grid.

Similar contour maps for the maximum lift angle of the UMC profile are presented in Figs. 13a and 13b with and without grid, respectively. Again, the local maximum can be found in the top-right-hand corner of each map, suggesting that the optimum LEU for the maximum lift angle should also have greater wavelength and amplitude with or without grid.

2. *Maximum Noise Reduction*

Figure 14 shows the overall sound power level (OAPWL) of the UMC profile with three different wavelengths as a function of the effective angle of attack α_{eff}, which are compared with the baseline result. The noise-spectra bandwidth was again between 40 and 2000 Hz. With grid, these figures reveal that the LEU amplitude h/c is an important parameter in reducing the turbulence interaction noise, where noise reductions are seen with an increase in h/c. For "no grid" case, the noise reduction by the UMC profile depends on a combination of the LEU amplitude and wavelength as well as α_{eff}. In α_{eff} between 0 and 8°, where both the low-frequency noise due to flow separation/stall and the midfrequency noise due to an interaction between the Tollmien–Schlichting waves and the laminar separation bubble (TS-SB noise) dominate, the UMC profile having $\lambda/c = 20$ and 30% with $h/c = 6\%$ (see Fig. 14b) and all the λ tested with $h/c = 12\%$ (Fig. 14c) are effective in reducing the overall noise. In α_{eff} between 8 and 12°, around which stall takes place, the overall noise appears to increase by all LEUs.

To show the noise-reduction performance of LEUs at an angle of attack of $\alpha_{\mathrm{eff}} = 15°$, contours of the percentage noise change of the UMC profile with grid is plotted in Fig. 15. It shows that optimal LEU parameters are located at around $\lambda/c = 15\%$ and $h/c = 10\%$. However, both the wavelength and amplitude are not very sensitive to noise reduction because the level differences are less than 1 dB across the entire contour map. We can, therefore, conclude that a combination of $\lambda/c = 30\%$ and $h/c = 6\%(\lambda 30h6)$ are good compromise parameters for LEU optimization considering the aerodynamic performance as well as the noise reduction near stall angle.

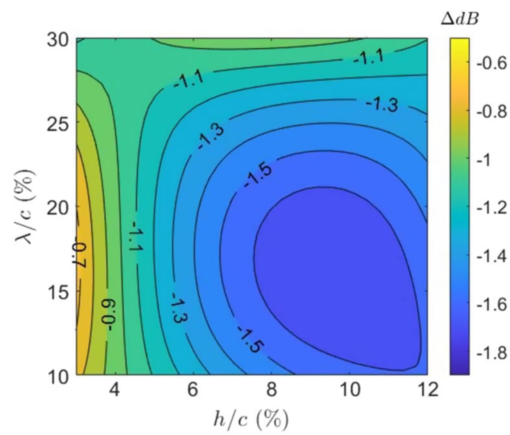

Fig. 15 Contours of the noise change in dB by the UMCs at $\alpha_{\mathrm{eff}} = 15°$ with grid.

D. Flow over an Optimized Airfoil

Figures 16a and 16b show the time-averaged streamlines (in pink) and the mean velocity contours (in blue) from the PIV measurement of flow over an optimized airfoil ($h/c = 6\%$ and $\lambda/c = 30\%$). The angle of attack was set at $\alpha = 10.8$ and 15.3°, where the boundary-layer thickness was $\delta = 7.5$ and 12.0 mm, respectively, at

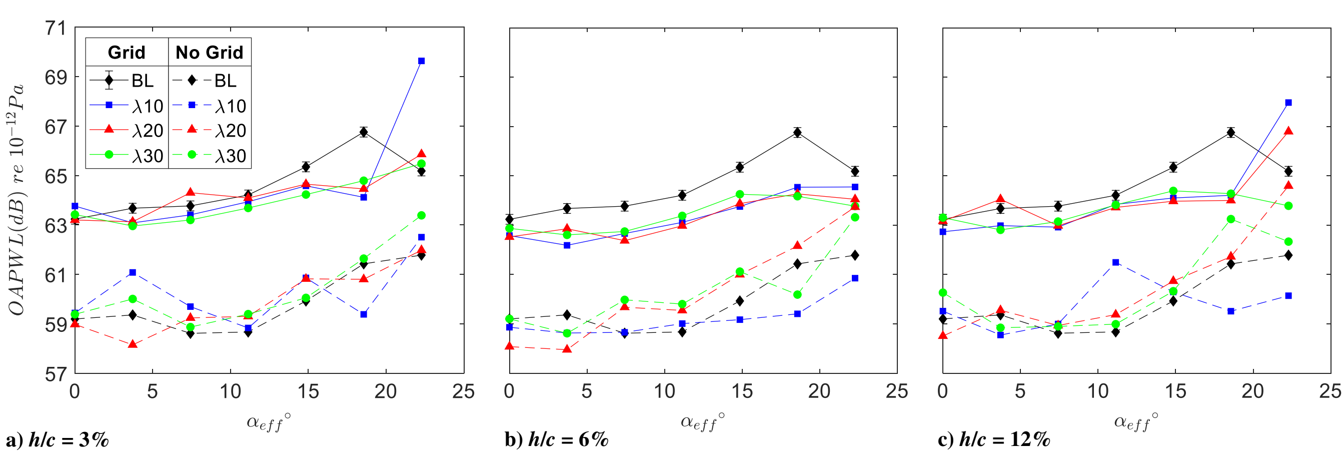

Fig. 14 Variations of overall sound power level with an angle of attack: a) $h/c = 3\%$; b) $h/c = 6\%$; c) $h/c = 12\%$.

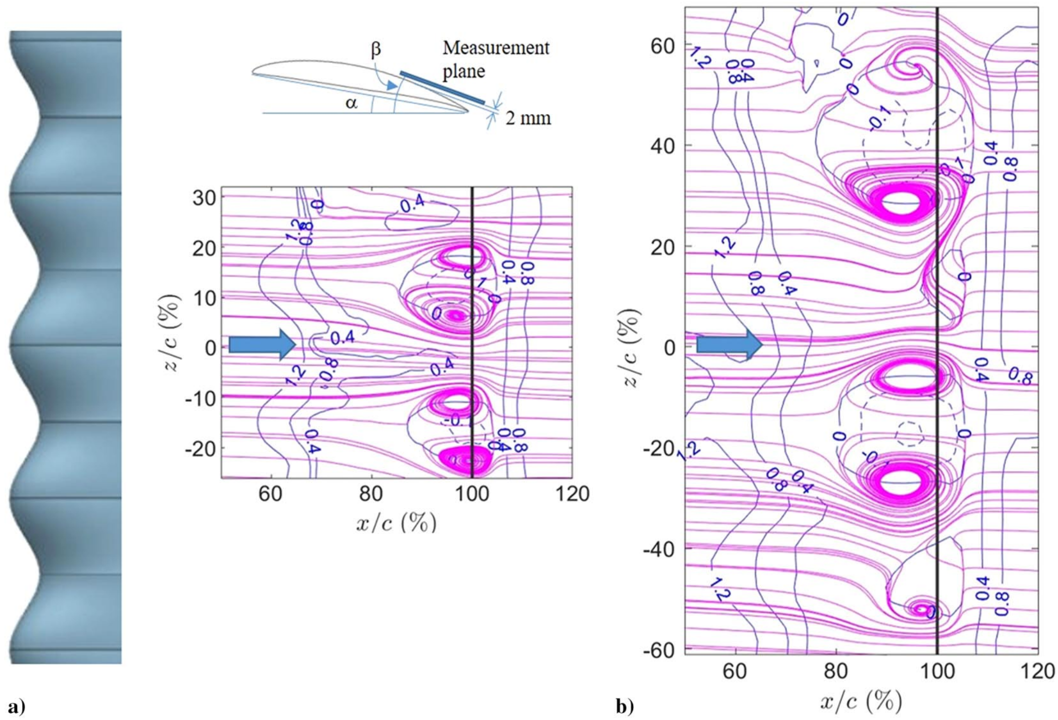

Fig. 16 Time-averaged streamlines (in pink) and $\bar{U}/\bar{U}_\infty$ contours (in blue) for $\alpha = 10.8°$ with $\beta = 23°$ (a) and $\alpha = 15.3°$ with $\beta = 35°$ (b).

$x/c = 0.75$. The freestream velocity was $U_\infty = 10$ m/s. The plane of the PIV measurement is defined in Fig. 16, where the distance between the model and the measurement plane was 2 mm. Peaks and troughs of the LEU are shown on the left, and the flow is from left to right. A comparison of flow recirculation regions downstream of the peak and the trough section of the LEU at $\alpha = 10.8°$ (see Fig. 16b) suggests that the flow separation takes place further downstream along the LEU peaks [26], as it has a higher velocity. Stall cells appear downstream of troughs, consisting of a pair of counter-rotating wall-normal vortices [20,24,25]. At this angle of attack, stall cells have the same periodicity as the wavelength of the LEU (see Fig. 16a). As the angle of attack is increased to $\alpha = 15.3°$, the streamwise as well as spanwise size of stall cells is increased by merging/absorbing neighboring stall cells as shown in Fig. 16b. The PIV result suggests that large stall cells are formed downstream of every other LEU trough at this angle of attack. A similar structure of stall cells was reported over an airfoil with LEUs [5,21].

Figures 17a and 17b are turbulence intensity contours over the optimized UMC profile ($\lambda30h6$) at $\alpha = 15.3°$ with grid, downstream of the LEU peak ($z/c = 0\%$) and the trough ($z/c = 15\%$), respectively. Figure 17a shows that the separating shear layer coming off the peak section of the LEU has a higher turbulence intensity than that along the trough section (see Fig. 17b). To understand this difference in the turbulence intensity, the velocity signal downstream of the LEU peak at the point of maximum turbulence intensity (marked "X" in Fig. 17a) is examined in Fig. 18a. For the nondimensional time $tU_\infty/c < 20$ and $tU_\infty/c > 120$, the streamwise velocity fluctuation appears to have a relatively low frequency with a large amplitude. For the rest of the time ($20 < tU_\infty/c < 120$), however, the frequency of the velocity fluctuation is increased and the amplitude reduced.

The unsteady nature of this velocity signal in Fig. 18a can be studied by wavelet spectra, which is given in Fig. 18b. Here, we used generalized Morse wavelets defined by $\Psi_{P,\gamma}(\omega) = U(\omega)a_{P,\gamma}\omega^{P^2/}e^{-\omega^{\gamma}}$ in the frequency domain ω, where $U(\omega)$ is the unit step function and $a_{P,\gamma}$ is a normalising constant [47]. The symmetry parameter and the time-bandwidth product were set to $\gamma = 3$ and $P^2 = 60$, respectively.

As shown in Fig. 19a, the flow over the airfoil is separated downstream of the LEU peak at the start of the signal ($0 < tU_\infty/c < 20$), where the corresponding velocity is low (see Fig. 18a) with a low-frequency component between 20 and 130 Hz (see Fig. 18b). Then the flow is reattached to the airfoil at $tU_\infty/c = 20$ (see Figs. 18a and 19b), increasing the frequency by approximately twice to 30–270 Hz (see Fig. 18b). The spectrum is also broadened, suggesting that the flow becomes fully turbulent as the flow is attached over the airfoil. Attached flow continues until $tU_\infty/c = 120$ (see Fig. 19b), then the lower frequency contents (20–80 Hz) start to increase to indicate the initiation of flow detachment, although high-frequency energy

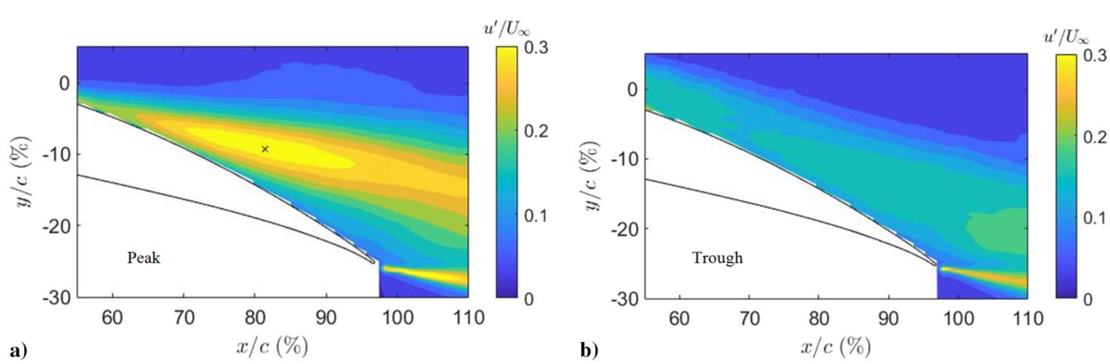

Fig. 17 Color contours of the turbulence intensity u'/U_∞ downstream of the LEU peak (a) and the trough (b) of an optimized LEU profile ($\lambda30h6$) at $\alpha = 15.3°$ with grid.

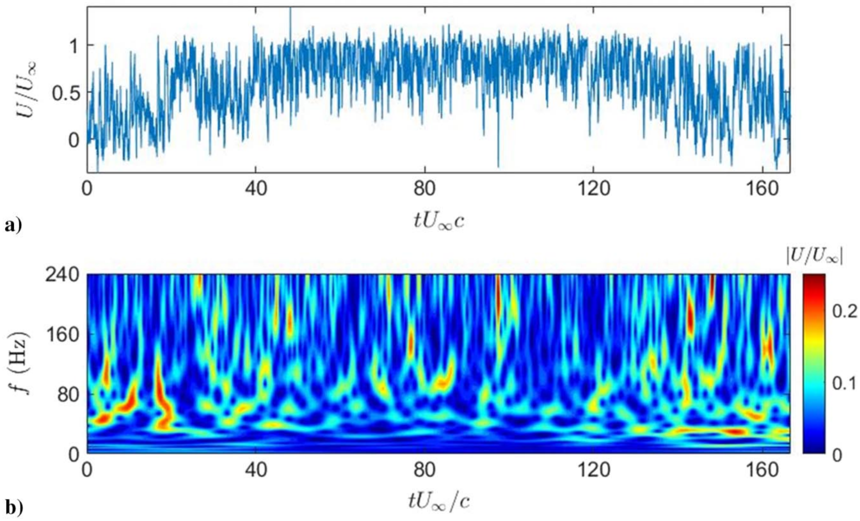

Fig. 18 The velocity fluctuation (a) at the point of maximum turbulence intensity in Fig. 17a and the corresponding wavelet spectrum (b).

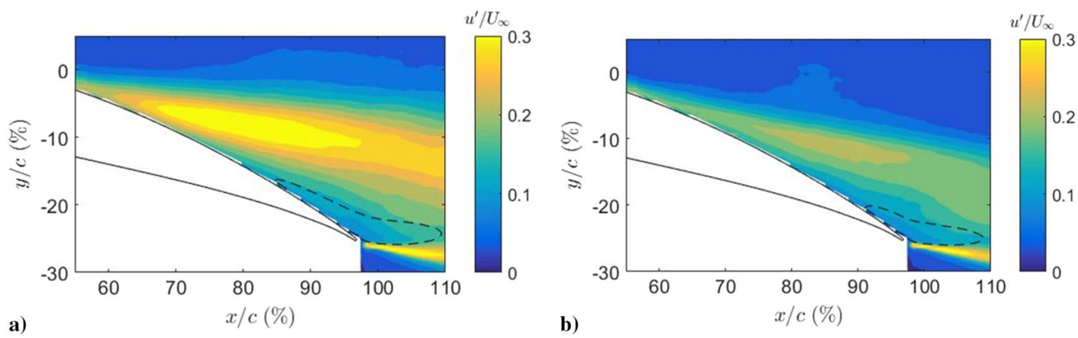

Fig. 19 Color contours of the turbulence intensity u'/U_∞ downstream of the LEU peak at $0 < tU_\infty/c < 20$ and $120 < tU_\infty/c < 165$ (a) and at $20 < tU_\infty/c < 120$ (b) of an optimized LEU profile ($\lambda 30h6$) at $\alpha = 15.3°$ with grid. The dotted lines indicate the region of flow separation with negative velocity.

contents up to 270 Hz are still present in the velocity signal until the end of this signal (see Figs. 18b and 19a). The velocity signal and its spectral behavior displayed in Figs. 18a and 18b suggest that the process of flow separation (detachment) process at around $tU_\infty/c = 120$ is much slower than that of flow reattachment ($tU_\infty/c = 20$). We believe that the unsteady nature of the velocity signal being observed here is related to the unsteadiness of stall-cell structures that have been observed by Cai et al. [20], whose position and shape changed with time as well as with the angle of attack.

IV. Conclusions

5 Optimization of the LEU of a NACA 65(12)-10 model was conducted in a wind tunnel at the effective Reynolds number of 10^6. Three leading-edge profiles were considered for this study. The cross-sectional shape of the Und1 profile is similar to that of the base line profile, whose leading edge always stays along the chord line within the LEU. On the other hand, the UAC profile is obtained by modifying only the 24% of the original leading-edge section by maintaining the similar shape. Here, the mean camber line of the UAC profile always stays on the original mean camber line within the LEU. Similar to the UAC profile, the leading-edge shape of the UMC profile changes only the front 24% of the original airfoil section. However, the leading edge of the UMC profile stays along the chord line within the LEU. Here it was found that the UMC profile could improve the $C_{L,\max}$ value without sacrificing the C_D unlike the LEUs on NACA 634-021 airfoil reported in [7]. Such an improvement in aerodynamic performance by the LEUs has never been demonstrated before. The noise reduction effects by the LEUs are seen in the entire frequencies near stall angles except for near $St = 1$. At low angles of attack, there is as much noise increase in the lower range of St, whereas there are small decreases in higher St range.

Further studies on the UMC profile have been carried out to find the best combination of LEU amplitude h and wavelength λ using a 3×3 test matrix in h (3, 6, and 12%, chord) and λ (10, 20, and 30% chord). The contour maps were obtained by interpolating nine measured $C_{L,\max}$ values, from which it was concluded that the optimum LEU for $C_{L,\max}$ should have greater wavelength and amplitude. A similar conclusion was made for the maximum lift angle of the UMC profile that the optimum LEU for the maximum lift angle should also have greater wavelength and amplitude. As for the noise-reduction performance of LEUs at $\alpha_{\text{eff}} = 15°$, the optimal LEU parameters were located at around $\lambda/c = 15\%$ and $h/c = 10\%$, although both the wavelength and amplitude were not very sensitive to noise reduction. It is therefore concluded that a combination of $\lambda/c = 30\%$ and $h/c = 6\% (\lambda 30h6)$ gives an optimum LEU for the UMC model for aerodynamic as well as aeroacoustic performance near stall angles. The optimal design proposed in this paper is mostly focused on high angle of attack where some degree of flow separation is present. A significant component of the noise reduction mechanism is therefore related to the degree by which flow separation can be suppressed by the leading-edge serration. Our optimal design therefore cannot be directly compared against the optimal designs proposed by Lyu et al. [48], which are obtained from a theoretical flat plate models in which the incoming turbulent flow ensures that the boundary layer remains fully attached.

PIV measurements of the flow over a NACA 65(12)-10 airfoil with an optimized LEU showed stall cells downstream of troughs at $\alpha = 10.8°$, consisting of a pair of counter-rotating wall-normal vortices. In other words stall cells at this angle of attack had the same periodicity as the wavelength of the LEU. As the angle of attack was increased to $\alpha = 15.3°$, the streamwise as well as spanwise size of stall cells was increased by merging/absorbing neighboring stall cells. Similar flow structures revealed by the PIV measurements may indicate the universality of the stall cell structure produced by the LEUs. The unsteady velocity signal at this angle of attack seems to be related to the unsteady stall-cell structures, where the turbulence produced at LEU peaks through a generation of streamwise vortices help reattach the flow whenever it is separated.

This paper resulted from a recently concluded multi-institutional project, where the optimization of LE undulations was investigated to
6 maximize noise reductions over a wide range of angles of attack without causing significant degradations in aerodynamic performance. This project was conducted with the aim that the optimized configuration and geometry of the LE profile will pave the way for a development of the next generation of quiet and more aerodynamically efficient airfoils. Here, the authors had aeroengine application in mind, which led to the choice of NACA 65(12)-10 airfoil shape for this investigation. This collaborative research was made possible by bringing together scientists and engineers with diverse background and expertise in fluid mechanics, aerodynamics, and aeroacoustics from four universities.

Acknowledgments

This study was supported by Engineering and Physical Sciences
7 Research Council (Grant No. EP/N018486/1). Some of the materials in this paper have been presented at the 23rd International Congress on Acoustics, Aachen, Germany, September 9–13, 2019.

References

[1] Choi, H., Park, H., Sagong, W., and Lee, S.-I., "Biomimetic Flow Control Based on Morphological Features of Living Creatures," *Physics of Fluids*, Vol. 24, No. 12, 2012, Paper 121302.
https://doi.org/10.1063/1.4772063

[2] Fish, F. E., and Lauder, G. V., "Passive and Active Flow Control by Swimming Fishes and Mammals," *Annual Review of Fluid Mechanics*, Vol. 38, 2006, pp. 193–224.
8 https://doi.org/10.1146/annurev.fluid.38.050304.092201

[3] Fish, F. E., and Battle, J. M., "Hydrodynamic Design of the Humpback Whale Flipper," *Journal of Morphology*, Vol. 225, No. 1, 1995, pp. 51–60.
https://doi.org/10.1002/jmor.1052250105

[4] Miklosovic, D. S., Murray, M. M., Howle, L. E., and Fish, F. E., "Leading-Edge Tubercles Delay Stall on Humpback Whale (Megaptera novaeangliae) Flippers," *Physics of Fluids*, Vol. 16, No. 5, 2004, pp. L39–L42.
https://doi.org/10.1063/1.1688341

[5] Johari, H., Henoch, C., Custodio, D., and Levshin, A., "Effects of Leading-Edge Protuberances on Airfoil Performance," *AIAA Journal*, Vol. 45, No. 11, 2007, pp. 2634–2642.
https://doi.org/10.2514/1.28497

[6] Custodio, D., Henoch, C. W., and Johari, H., "Aerodynamic Characteristics of Finite Span Wings with Leading-Edge Protuberances," *AIAA Journal*, Vol. 53, No. 7, 2015, pp. 1878–1893.
https://doi.org/10.2514/1.J053568

[7] Wei, Z. Y., Toh, J. W. A., Ibrahim, I. H., and Zhang, Y. N., "Aerodynamic Characteristics and Surface Flow Structures of Moderate Aspect-Ratio Leading-Edge Tubercled Wings," *European Journal of Mechanics B - Fluids*, Vol. 75, 2019, pp. 143–152.
https://doi.org/10.1016/j.euromechflu.2019.01.001

[8] Hansen, K. L., Kelso, R. M., and Dally, B. B., "Performance Variations of Leading-Edge Tubercles for Distinct Airfoil Profiles," *AIAA Journal*, Vol. 49, No. 1, 2011, pp. 185–194.
https://doi.org/10.2514/1.J050631

[9] Rostamzadeh, N., Kelso, R. M., Dally, B. B., and Hansen, K. L., "The Effect of Undulating Leading-Edge Modifications on NACA 0021 Airfoil Characteristics," *Physics of Fluids*, Vol. 25, No. 11, 2013, Paper 117101.
https://doi.org/10.1063/1.4828703

[10] Guerreiro, J. L. E., and Sousa, J. M. M., "Low-Reynolds-Number Effects in Passive Stall Control Using Sinusoidal Leading Edges," *AIAA Journal*, Vol. 50, No. 2, 2012, pp. 461–469.
https://doi.org/10.2514/1.J051235

[11] Corsini, A., Delibra, G., and Sheard, A. G., "On the Role of Leading-Edge Bumps in the Control of Stall Onset in Axial Fan Blades," *Journal of Fluids Engineering*, Vol. 135, No. 8, 2013.
https://doi.org/10.1115/1.4024115 9

[12] Corsini, A., Delibra, G., and Sheard, A. G., "The Application of Sinusoidal Blade-Leading Edges in a Fan-Design Methodology to Improve Stall Resistance," *Proceedings of the Institution of Mechanical Engineers, Part A: Journal of Power and Energy*, Vol. 228, No. 3, 2014, pp. 255–271.
https://doi.org/10.1177/0957650913514229

[13] Wei, Z., Lian, L., and Zhong, Y., "Enhancing the Hydrodynamic Performance of a Tapered Swept-Back Wing Through Leading-Edge Tubercles," *Experiments in Fluids*, Vol. 59, No. 6, 2018, p. 103.
https://doi.org/10.1007/s00348-018-2557-5

[14] Aftab, S. M. A., Razak, N. A., Rafie, A. S. M., and Ahmad, K. A., "Mimicking the Humpback Whale: An Aerodynamic Perspective," *Progress in Aerospace Sciences*, Vol. 84, 2016, pp. 48–69.
https://doi.org/10.1016/j.paerosci.2016.03.002

[15] Stalnov, O., and Chong, T. P., "Scaling of Lift Coefficient of an Airfoil with Leading-Edge Serrations," *AIAA Journal*, Vol. 57, No. 8, 2019, pp. 3615–3619.
https://doi.org/10.2514/1.J058168

[16] Polacsek, C., Reboul, G., Clair, V., Garrec, T., Dufour, G., and Deniau, H., "Turbulence-Airfoil Interaction Noise Reduction Using Wavy Leading Edge: An Experimental and Numerical Study," *Noise Control Engineering of Japan (INCE/J) and Acoustical Society of Japan (ASJ)*, Osaka, 2011, pp. 1–11. 10

[17] Chaitanya, P., Joseph, P., Narayanan, S., Vanderwel, C., Turner, J., Kim, J. W., and Ganapathisubramani, B., "Performance and Mechanism of Sinusoidal Leading Edge Serrations for the Reduction of Turbulence-Aerofoil Interaction Noise," *Journal of Fluid Mechanics*, Vol. 818, 2017, pp. 435–464.
https://doi.org/10.1017/jfm.2017.141

[18] Hansen, K., Kelso, R., and Doolan, C., "Reduction of Flow Induced Airfoil Tonal Noise Using Leading Edge Sinusoidal Modifications," *Acoustics Australia*, Vol. 40, No. 3, 2012, pp. 172–177.

[19] Chong, T. P., Vathylakis, A., McEwen, A., Kemsley, F., Muhammad, C., and Siddiqi, S., "Aeroacoustic and Aerodynamic Performances of an Aerofoil Subjected to Sinusoidal Leading Edges," *21st AIAA/CEAS Aeroacoustics Conference*, 2015. 11

[20] Cai, C., Zuo, Z., Maeda, T., Kamada, Y., Li, Q. A., Shimamoto, K., and Liu, S., "Periodic and Aperiodic Flow Patterns Around an Airfoil with Leading-Edge Protuberances," *Physics of Fluids*, Vol. 29, No. 11, 2017, Paper 115110.
https://doi.org/10.1063/1.4991596

[21] Skillen, A., Revell, A., Pinelli, A., Piomelli, U., and Favier, J., "Flow over a Wing with Leading-Edge Undulations," *AIAA Journal*, Vol. 53, No. 2, 2015, pp. 464–472.
https://doi.org/10.2514/1.J053142

[22] Zhang, M. M., Wang, G. F., and Xu, J. Z., "Aerodynamic Control of Low-Reynolds-Number Airfoil with Leading-Edge Protuberances," *AIAA Journal*, Vol. 51, No. 8, 2013, pp. 1960–1971.
https://doi.org/10.2514/1.J052319

[23] Zhang, M. M., Wang, G. F., and Xu, J. Z., "Experimental Study of Flow Separation Control on a Low-Re Airfoil Using Leading-Edge Protuberance Method," *Experiments in Fluids*, Vol. 55, No. 4, 2014. ARTN 1710
https://doi.org/10.1007/s00348-014-1710-z

[24] Zhao, M., Zhang, M., and Xu, J., "Numerical Simulation of Flow Characteristics Behind the Aerodynamic Performances on an Airfoil with Leading Edge Protuberances," *Engineering Applications of Computational Fluid Mechanics*, Vol. 11, No. 1, 2017, pp. 193–209.
https://doi.org/10.1080/19942060.2016.1277165

[25] Malipeddi, A. K., Mahmoudnejad, N., and Hoffmann, K., "Numerical Analysis of Effects of Leading-Edge Protuberances on Aircraft Wing Performance," *Journal of Aircraft*, Vol. 49, 2012, pp. 1336–1344.
https://doi.org/10.2514/1.C031670

[26] Hansen, K. L., Rostamzadeh, N., Kelso, R. M., and Dally, B. B., "Evolution of the Streamwise Vortices Generated Between Leading Edge Tubercles," *Journal of Fluid Mechanics*, Vol. 788, 2016, pp. 730–766.
https://doi.org/10.1017/jfm.2015.611

[27] Wang, S., Zhou, Y., Alam, M. M., and Yang, H., "Turbulent Intensity and Reynolds Number Effects on an Airfoil at Low Reynolds Numbers," *Physics of Fluids*, Vol. 26, No. 11, 2014, Paper 115107.
https://doi.org/10.1063/1.4901969

[28] Kurian, T., and Fransson, J. H. M., "Grid-Generated Turbulence Revisited," *Fluid Dynamics Research*, Vol. 41, No. 2, 2009, Paper 021403.
https://doi.org/10.1088/0169-5983/41/2/021403

[29] Nakamura, Y., and Ozono, S., “The Effects of Turbulence on a Separated and Reattaching Flow,” *Journal of Fluid Mechanics*, Vol. 178, 1987, pp. 477–490.
https://doi.org/10.1017/S0022112087001320
[30] Mueller, T. J., “Low Reynolds Number Vehicles,” AGARD AG-288, 1985.
[31] Moffat, R. J., “Describing the Uncertainties in Experimental Results,” *Experimental Thermal and Fluid Science*, Vol. 1, No. 1, 1988, pp. 3–17.
https://doi.org/10.1016/0894-1777(88)90043-X
[32] Westerweel, J., “Theoretical Analysis of the Measurement Precision in Particle Image Velocimetry,” *Experiments in Fluids*, Vol. 29, No. 1, 2000, pp. S003–S012.
https://doi.org/10.1007/s003480070002
[33] Qu, W., Xiong, J., Chen, S., and Cheng, X., “High-Fidelity PIV Measurement of Cross Flow in 5×5 Rod Bundle with Mixing Vane Grids,” *Nuclear Engineering and Design*, Vol. 344, 2019, pp. 131–143.
https://doi.org/10.1016/j.nucengdes.2019.01.021
[34] Brooks, T. F., Marcolini, M. A., and Pope, D. S., “Airfoil Trailing Edge Flow Measurements and Comparison with Theory Incorporating Open Wind Tunnel Corrections,” AIAA Paper 1984-2266, 1984.
https://doi.org/10.2514/6.1984-2266
[35] Chong, T. P., Joseph, P. F., and Davies, P. O. A. L., “Design and Performance of an Open Jet Wind Tunnel for Aero-Acoustic Measurement,” *Applied Acoustics*, Vol. 70, No. 4, 2009, pp. 605–614.
https://doi.org/10.1016/j.apacoust.2008.06.011
[36] Lacagnina, G., Chaitanya, P., Berk, T., Kim, J.-H., Joseph, P., Ganapathisubramani, B., Hasheminejad, S. M., Chong, T. P., Stalnov, O., Choi, K.-S., Shahab, M. F., Omidyeganeh, M., and Pinelli, A., “Mechanisms of Airfoil Noise Near Stall Conditions,” *Physical Review Fluids*, Vol. 4, No. 12, 2019, Paper 123902.
https://doi.org/10.1103/PhysRevFluids.4.123902
[37] Feng, L.-H., Choi, K.-S., and Wang, J.-J., “Flow Control over an Airfoil Using Virtual Gurney Flaps,” *Journal of Fluid Mechanics*, Vol. 767, 2015, pp. 595–626.
https://doi.org/10.1017/jfm.2015.22
[38] Laitone, E. V., “Wind Tunnel Tests of Wings at Reynolds Numbers Below 70 000,” *Experiments in Fluids*, Vol. 23, No. 5, 1997, pp. 405–409.
https://doi.org/10.1007/s003480050128
[39] Ohtake, T., Nakae, Y., and Motohashi, T., “Nonlinearity of the Aerodynamic Characteristics of NACA0012 Aerofoil at Low Reynolds Numbers,” *Journal of the Japan Society for Aeronautical And Space Sciences*, Vol. 55, No. 644, 2007, pp. 439–445.
https://doi.org/10.2322/jjsass.55.439
[40] Winslow, J., Otsuka, H., Govindarajan, B., and Chopra, I., “Basic Understanding of Airfoil Characteristics at Low Reynolds Numbers (104–105),” *Journal of Aircraft*, Vol. 55, No. 3, 2018, pp. 1050–1061.
https://doi.org/10.2514/1.C034415
[41] Arena, A. V., and Mueller, T. J., “Laminar Separation, Transition, and Turbulent Reattachment Near the Leading Edge of Airfoils,” *AIAA Journal*, Vol. 18, No. 7, 1980, pp. 747–753.
https://doi.org/10.2514/3.50815
[42] Hansen, K., Kelso, R., Choudhry, A., and Arjomandi, M., “Laminar Separation Bubble Effect on the Lift Curve Slope of an Airfoil,” *19th Australasian Fluid Mechanics Conference*. 2014.
[43] Lissaman, P. B. S., “Low-Reynolds-Number Airfoils,” *Annual Review of Fluid Mechanics*, Vol. 15, 1983, pp. 223–239.
https://doi.org/10.1146/annurev.fl.15.010183.001255
[44] Gaster, M., “The Structure and Behaviour of Separation Bubbles,” ARC R&M 3595, 1967.
[45] Horton, H. P., “A Semi-Empirical Theory for the Growth and Bursting of Laminar Separation Bubbles,” ARC CP 1073, 1969.
[46] Chong, T. P., and Joseph, P. F., “An Experimental Study of Airfoil Instability Tonal Noise with Trailing Edge Serrations,” *Journal of Sound and Vibration*, Vol. 332, No. 24, 2013, pp. 6335–6358.
https://doi.org/10.1016/j.jsv.2013.06.033
[47] Lilly, J. M., and Olhede, S. C., “Generalized Morse Wavelets as a Superfamily of Analytic Wavelets,” *IEEE Transactions on Signal Processing*, Vol. 60, No. 11, 2012, pp. 6036–6041.
https://doi.org/10.1109/TSP.2012.2210890
[48] Lyu, B., Ayton, L. J., and Chaitanya, P., “On the Acoustic Optimality of Leading-Edge Serration Profiles,” *Journal of Sound and Vibration*, Vol. 462, 2019, Paper 114923.
https://doi.org/10.1016/j.jsv.2019.114923

P. Lavoie
Associate Editor

Queries

1. AU: Please check that the copyright (©) type is correct. Please note that the code will be added upon publication.
2. AU: References have been renumbered for chronologic order of citations in the text. Please check.
3. AU: Please define FS.
4. AU: "We can, therefore, conclude that a combination of $\lambda/c = 30\%$ and $h/c = 6\%$ ($\lambda 30h6$) are good compromise parameters" is not clear. Please review and edit as necessary.
5. AU: Conclusions section has been edited to be in the third person, per journal guidelines. Please check that your meaning was retained.
6. AU: AoA has been expanded as angles of attack. Please check.
7. AU: EPSRC has been expanded as Engineering and Physical Sciences Research Council. Please check.
8. AU: Please provide the issue number and/or month of publication for Refs. [2, 7, 14, 17, 25, 26, 29, 33, 37, 43, 48] if applicable.
9. AU: For Refs. [11, 23], please provide the page range.
10. AU: For Ref. [16], please provide the full name and location of the publisher (NOT the conference host).
11. AU: If Refs. [19, 42] are published proceedings, please provide the names and locations of the publishers (NOT of the conference hosts) and the page ranges. If they are conference papers, please provide the paper numbers and the organizers' names.

Funding Information

The following research funding sources have been associated with your manuscript:

- EPSRC; Award no. EP/N018486/1

Funding sources listed here can be 1) research grants from outside agencies or organizations or 2) if an author is employed by a U.S. government agency that directly funded this research, this employer also may be listed here as a funding agency. Please confirm that this information is complete and correct for all authors. Edit the Funding Data/Acknowledgments section of your paper if you have changes to funding agency names or grant numbers. Use the funder's full and official name.